Applied Catalysis B: Environmental 340 (2024) 123176

Contents lists available at ScienceDirect

Applied Catalysis B: Environmental

journal homepage: www.elsevier.com/locate/apcatb

NiSn intermetallic nanoparticles with geometrically isolated Ni sites for selective C-O cleavage of furfural

Feifei Yang [a], Tianyu Zhang [b,*], Jiankang Zhao [c,*], Wei Zhou [a,*], Nicole J. Libretto [d], Jeffrey T. Miller [d]

[a] School of Chemical Engineering and Technology, China University of Mining and Technology, Xuzhou, Jiangsu 221116, China
[b] College of Environmental Science and Engineering, Beijing Forestry University, Beijing 100083, China
[c] Hefei National Laboratory for Physical Sciences at the Microscale, University of Science and Technology of China, Hefei 230026, China
[d] Davidson School of Chemical Engineering, Purdue University, West Lafayette, IN 47907, United States

ARTICLE INFO

Keywords:
Furfural hydrodeoxygenation
Ni_3Sn
Geometric isolated
Electronic modification
Selective C-O cleavage

ABSTRACT

Selective C-O bond cleavage is critical in upgrading biomass derivatives to chemicals and fuels. However, eliminating side reactions from the aromatic rings is challenging, in large part because of the difficulty in precisely modulating the local atomic structure of the active sites. Herein, we report a Ni_3Sn intermetallic nanoparticle with geometrically isolated Ni sites for hydrodeoxygenation of furfural, which shows considerable activity and 91 % selectivity toward 2-methylfuran at 96 % conversion, in stark contrast to the performance of Ni nanoparticle that mainly produces furan, CH_4 and C4 products derived from the ring chemistry. Experimental and theoretical calculations demonstrate that the isolated Ni sites in Ni_3Sn surface limits the furan ring interaction, while the electron donation from Sn to Ni facilitates the carbonyl O bonding to Ni sites. It therefore prevents side reactions from ring chemistry, but allows a facile sequential reaction of selective carbonyl hydrogenation followed by C-OH scission to 2-methylfuran.

1. Introduction

Lignocellulosic biomass is a widely available, potentially carbon-neutral and renewable carbon source for the production of transportation fuels and commodity chemicals, in response to the rising environmental and energy challenges [1,2]. Furfurals represent a significant family of aromatic compounds produced via dehydration and hydrolysis of xylose, which have been identified as valuable fuel precursors to produce methylated furans as the target fuel products or fuel additives [3–5]. The major barrier in converting furfurals into fuels is to selective hydrogenation and hydrogenolysis of the C═O bond in the carbonyl while preserving C-C bonds. Therefore, there is ongoing interest to understand the hydrodeoxygenation (HDO) mechanism and optimize the active center [6–12].

The primary goal is to preferentially activate the carbonyl group of furfural (FAL), while minimizing furan ring reactions from the ring chemistry, i.e., ring hydrogenation, decarbonylation, or hydrogenolysis et al. [13–16]. Bimetallic catalysts often display improved activity and selectivity owning to the unique interaction and/or synergy effect between the two metals [17]. Several studies have reported that the side ring chemistry can be suppressed by alloying a group 10 metal (such as Pt, Pd, Ni) with a second more oxophilic metal (such as Cu, Fe, Co, Zn) [18–27], as the oxophilic metal improves the adsorption strength of carbonyl in FAL, while limiting the furan ring adsorption [19,20]. Ni-based bimetallic catalysts are cheaper, non-noble metal based alternatives to traditional Pt and Pd-based catalysts, however, their catalytic performance is still insufficient and further improvements in selectivity are needed.

The poor selectivity of monometallic Ni for HDO of FAL can be ascribed to the presence of Ni ensembles on the catalyst surface [26,27]. For instance, Christopher et al. reported that the NiCu alloy catalyst with low surface Cu leads to furan ring interaction with Ni ensemble, resulting in furan ring hydrogenation as the dominating path for HDO of FAL at 200 °C and 2.5 MPa H_2. On the other hand, NiCu alloy with Cu enriched surface demonstrates ~88 % selectivity to the desirable 2-methylfuran (MF) product at ~100 % conversion [26]. Similarly, Wei et al. have also reported that a NiMo alloy is unselective to MF and 2-methyltetrahydrofuran (MTHF) for FAL HDO at 200 °C and 0.1 MPa

* Corresponding authors.
E-mail addresses: tzhang@bjfu.edu.cn (T. Zhang), jkzhao20@ustc.edu.cn (J. Zhao), zhouwei@cumt.edu.cn (W. Zhou).

https://doi.org/10.1016/j.apcatb.2023.123176
Received 15 April 2023; Received in revised form 7 August 2023; Accepted 11 August 2023
Available online 12 August 2023
0926-3373/© 2023 Elsevier B.V. All rights reserved.

H_2, whereas the Mo enriched NiMo intermetallic compound displays ~98.3 % MF selectivity at ~100 % conversion [27]. Therefore, restricting the size of the active sites in a Ni containing catalyst, especially isolation of Ni sites, and thereby preventing the formation of ensembles of neighboring Ni atoms on the surface may yield preferred MF selectivity. The active site isolation increases Ni-Ni distances and may lead to weakly π bonded or even un-bonded furan on top of an isolated Ni atom [28,29], which offers a promising direction in tuning MF selectivity for HDO of FAL over Ni alloy catalysts. Nevertheless, more studies are required on rational control of the atomically structure of the active center to fully understand the structure-activity relationship at atomical level.

Sn is known to be an effective additive to isolate the aggregated Ni atoms through forming NiSn intermetallic compounds. Moreover, the Sn alloyed Ni catalyst has been widely used in reforming and dehydrogenation reactions and showed positive effect towards enhanced selectivity and catalyst stability by inhibition of side reactions like cracking and carbon nucleation on the Ni active center [30–32]. Considering these positive effects of Sn in modifying Ni active sites, it is therefore of great interest to explore its potential role in regulating the catalytic performance during HDO of FAL on Ni based catalysts.

In this work, a Ni_3Sn intermetallic catalyst with geometrically isolated Ni sites was developed for HDO of FAL. It displays considerable activity and high selectivity (91 % at 96 % conversion) toward FAL deoxygenation to MF, in stark contrast to the monometallic Ni catalyst, which mainly catalyzes C-C hydrogenolysis and ring opening to produce furan, CH_4 and C_4 products. Meanwhile, a nanosized Ni_3Sn_2 intermetallic was also investigated, which also shows high MF selectivity, but low activity. Using a combination of detailed characterizations and density functional theoretical calculation, the role of Sn as well as the reaction mechanism for HDO of FAL on the isolated Ni center were revealed.

2. Experimental section

2.1. Sample preparation

Chemicals were purchased from Sigma-Aldrich. The following catalysts were prepared: (1) 2 wt% Ni/SiO_2 (named as Ni) was prepared by incipient wetness impregnation method. Typically, 1 g SiO_2 (with a surface area of 200 m^2/g) was impregnated with 3 mL aqueous solution of $Ni(NO_3)_2{\cdot}6\ H_2O$ for 24 h. The sample was subsequently dried at 120 °C for 12 h, and further calcined in air at 400 °C for 4 h. (2) Sn/SiO_2 was prepared by a surface organometallic chemistry method, which could lead to a high dispersion of Sn on the SiO_2 support [33]. Typically, 34.5 or 69 mg of dimethyltin dichloride (to obtain a Sn loading of 1.8 or 3.7 wt%, respectively) was dissolved in 25 mL anhydrous toluene, followed by adding 1 g SiO_2 and stirred at room temperature for 2 h. Then 2.5 mL triethylamine was added to the mixture and further stirred for another 5 h. The mixture was then filtered, washed with ethanol, dried at 120 °C for 12 h, and finally calcined at 580 °C for 3 h in flowing air (100 mL/min) (Fig. S1). (3) 2 wt%Ni-1.8 wt%Sn/SiO_2 (named as $NiSn_{0.4}$, where 0.4 refer to the Sn/Ni molar ratio) was prepared by incipient wetness impregnation. Briefly, the as-prepared 1.8 wt% Sn/SiO_2 was impregnated with aqueous solution of $Ni(NO_3)_2{\cdot}6\ H_2O$, with the same treatment conditions as that of Ni/SiO_2. (4) 2 wt%Ni-3.7 wt%Sn/SiO_2 (named as $NiSn_{0.9}$, where 0.9 refer to the Sn/Ni molar ratio) were prepared as that of $NiSn_{0.4}$ expected with 3.7 wt% Sn/SiO_2.

2.2. Catalyst characterization

The Ni and Sn concentrations in samples were determined by inductively coupled plasma atomic emission spectroscopy (ICP-AES) with an ICP-AES 7300DV instrument. Before the measurement, about 100 mg of the sample was dissolved in HF aqueous solution, the excessive amount of boric acids solution were added to form a mixture. The real loadings were determined to be within a ± 10 % error of the nominated loadings (as seen in Table S1).

X-ray diffraction patterns were conducted on a Rigaku D/max 2500 diffractometer with Cu (Kα) radiation source at a rate of 2°/min with the step width of 0.0195°. High-angle annular dark field scanning transmission electron microscopy (HAADF-STEM) images were collected on a JEOL JEM-2100 F microscope operating at 200 kV.

H_2-temperature programed reduction (H_2-TPR) was performed on Micrometrics AutoChem II 2910 equipped with a Mass Spectrometry (MS) detector (OmniStar). The catalyst was first pretreated at 300 °C for 1 h in He (30 mL/min) to remove H_2O and then cooled to room temperature. Then the gas was switched to 10 % H_2/Ar (30 mL/min). After reaching a stable base line, the sample was heated to 900 °C at a rate of 10 °C/min. The H_2 consumption was detected by a thermal conductivity detector.

In situ X-ray absorption spectroscopy (XAS) experiments were performed at the 10-BM beamline at the Advanced Photon Source (APS) at Argonne National Laboratory. Measurements were performed at the Ni K (8.333 keV) and Sn K (29.2000 keV) edges for each sample. Samples were pressed into a stainless-steel sample holder and placed in a quartz tube sample cell. The cell was sealed and treated at 400 °C in 3.5 % H_2/He, cooled to room temperature in He, and then transferred to the beamline. The measurements were performed in transmission mode from 250 eV below the edge to 550 eV above the edge, which took approximately 10 min per scan. This means that the scan ranges at the Ni and Sn edges were 8132–9000 eV and 28,950–30,000 eV, respectively. The data were interpreted using WinXAS 3.1 software to find the coordination number (CN) and bond distance (R) using standard fitting procedures.

X-ray photoelectron spectroscopy (XPS) was performed on a PHI 5800 ESCA system equipped with an Al Kα X-ray anode at 300 W and 15 kV. The catalyst was ex situ reduced at 400 °C for 1 h before measurement. Beside the concerned elements, the C 1 s spectra was recorded during all sample measurements, then the results were calibrated with the binding energy (BE) of 284.8 eV from C 1 s

In situ Diffuse Reflectance Infrared Fourier Transform spectra of CO adsorption (CO-DRIFTS) was recorded on a Bruker Equinox 55 spectrometer equipped with a mercury cadmium telluride (MCT) detector. The catalyst was first reduced in situ in the DRIFT cell in H_2 at 400 °C for 1 h, followed by purging with He for 0.5 h at the same temperature. The catalyst was then cooled to 20 °C by cooling water. A flow of CO was then introduced to the system until saturated adsorption, followed by He purging to remove the physical adsorbed CO.

CO microcalorimetric adsorption over reduced catalyst was measured at 40 °C on a BT 2.15 Calvet calorimeter connected to gas handling and volumetric systems equipped with MKS 698 A Baratron capacitance nanometers ($\pm 1.33 \times 10^{-2}$ Pa). Prior to CO adsorption, the catalyst was in situ reduced in H_2 at 400 °C for 1 h, followed by evacuation for 0.5 h. After cooling to room temperature in vacuum, the quartz tube was refilled with He and tightly sealed. Then the tube was transferred to the calorimetric cell and outgassed at 40 °C overnight. Pure CO was stepwise introduced to the catalyst up to a pressure of ~10 Torr at 40 °C.

H_2-D_2 exchange experiments were performed on the same Ominstar Micrometrics system. The fresh sample was reduced in H_2 at 400 °C for 1 h, followed by He purging for 0.5 h. After cooling to room temperature, D_2 and H_2 were then introduced to the system. Until a satisfactory signal/noise ratio, the sample was heated to 200 °C at a rate of 5 °C/min. The mass/charge ratio (m/z) values are 2 for H_2, 4 for D_2, and 3 for HD, respectively. After the temperature programmed surface reaction measurement, the sample was cooled to 70 °C under the same gas until the signals reach steady state. The semi-H_2 conversion was calculated based on H_2 ($m/z = 2$) MS intensity at the inlet (I_{in}) and outlet (I_{out}) of the catalyst, which is defined as $(I_{in}\text{-}I_{out})/I_{in}$ during H_2-D_2 exchange reaction at 70 °C.

O_2-Temperature programmed oxidation (O_2-TPO) was performed on

above system. The spend catalyst was heated from room temperature to 800 °C at a rate of 10 °C/min in flowing 5 %O_2/He, with the signal of m/z = 18, 28, 44 being recorded in MS detector.

2.3. Reactivity test

The vapor phase HDO of furfural (FAL) was conducted in a fixed-bed flow reactor at atmospheric pressure, equipped with online analysis by gas chromatography (GC9790plus, Zhejiang Fuli). The catalyst (40–60 mesh) was loaded on the top of a thermocouple between two layers of quartz wool in a quartz tube reactor (6 mm diameter). Prior to each run, the catalyst was reduced in situ at 400 °C for 1 h in H_2. Then, the temperature was cooled down to 250 °C in H_2 flow. FAL was purified by distillation to remove any residues and oligomers and then kept under He atmosphere until its use in the reaction test. The purified FAL was injected through a syringe pump (KDS100, kd scientific) and vaporized at 180 °C before entering the reactor. The H_2/FAL molar ratio was kept at 60 in all runs. The effluent was analyzed and quantified in the online GC. The components of the effluent were identified by off-line gas chromatography-mass spectrometry (GC-MS, Shimadzu QP2010S). The outlet was heated to 230 °C to avoid any product condensation. The space time (W/F, h) is defined as the ratio of catalyst mass (g) to FAL mass feed flow rate (g/h). The conversion and yield are reported in mol_{carbon}%. The carbon balance was checked to be > 90 % in every run.

2.4. DFT calculation

DFT calculations were performed using the Vienna Ab-initio Simulation Package (VASP) [34,35]. The core and valence electrons were represented by the projector augmented wave (PAW) method and plane-wave basis functions with a kinetic energy cut-off of 500 eV [36]. The generalized gradient approximation (GGA) with the Perdew-Burke-Ernzerhof (PBE) exchange-correlation functional was used in the calculations [37]. We tested the k-points by calculating the adsorption of furfural on Ni_3Sn(110). The adsorption energies of trans-furfural are − 0.80 eV, − 0.80 eV and − 0.79 eV with k-points of 2 × 2 × 1, 3 × 3 × 1, 4 × 4 × 1, respectively. To consider the computation accuracy and cost comprehensively, a Monkhorst-Pack grid of size of 2 × 2 × 1 was used to sample the surface Brillouin zone. Ground-state atomic geometries were obtained by minimizing the forces on the atoms below 0.02 eV/Å. The transition states were obtained using the climbing image nudged elastic band (CI-NEB) method by relaxing the force below 0.05 eV/Å.

According to the experimental characterization results, the Ni_3Sn intermetallic was used to model the bimetallic $NiSn_{0.4}$ catalyst. Bulk optimization yielded lattice parameters of a=b=c= 5.938 Å, in good agreement with the recent result [38]. The more preferential (110) surface, accordance to the (220) surface detected by XRD, was used to model the alloy catalyst surface, with five slabs of a 4 × 4 unit cell and the top two layers allowed relaxing in the calculations. A distance of 15 Å is added to the vacuum layer in the calculation to avoid the interaction between each slab.

The Gibbs free energy change in this work is defined as:

$$\Delta G = \Delta E + \Delta ZPE - T\Delta S$$

where ΔE is obtained from DFT calculations, ΔZPE is the correction in zero-point energies, and TΔS is the contribution of entropy. The entropy of adsorbed species is considered as 0 except for the vertically adsorbed furfural. The entropy of adsorbed furfural on Ni_3Sn(110) is simplified as about 2/3 of the gaseous furfural as only vertical translational degree of freedom is limited.

3. Results and discussion

3.1. Structure characterization of bimetallic NiSn/SiO_2 catalyst

XRD was used to identify the structure of the as-prepared catalysts after calcination (Fig. 1 A) and to compare monometallic Ni with bimetallic $NiSn_{0.4}$ and $NiSn_{0.9}$. The reflections at 37.2, 43.3 and 62.9° in all three samples are consistent with NiO. Scherrer analysis was performed on the 43.3° reflection of each diffraction pattern to determine the average NiO particle size, and the estimated particle size was between 10.1 and 12.5 nm for each catalyst, however, no trend was observed with increasing Sn concentration, possibly owing to the sequential loading method (Figs. S1–2). In addition, no Sn-related diffractions were observed in XRD, indicating that Sn species are highly dispersed.

The interaction between Ni and Sn was studied by H_2-TPR. As shown in Fig. 1B, the Ni catalyst displays two reduction peaks at 324 and 408 °C, owing to the sequential of partial and fully reduction of NiO to Ni metal, respectively [18]. Whereas the reduction of Sn requires a much higher temperature of > 850 °C, due to the strong interaction between Sn species and SiO_2 support [33]. The reducibility patterns of NiSn are very different from either Ni or Sn. At lower Sn content level, for $NiSn_{0.4}$, two reduction peaks are presented at 354 and 447 °C, including an additional shoulder at 524 °C. The first peak is due to the reduction of NiO, as the presence of Sn has been suggested to impede H_2 dissociation on Ni, and cause a delay in NiO reduction [30]. It is expected that the reduced Ni could further facilitate H_2 activation, and promote the co-reduction of Ni oxide and Sn oxide that closes to Ni particles (at 447 °C), while the shoulder peak (at 524 °C) may be the reduction of Sn oxide a little far from Ni (see the structure shown in Fig. S2). In addition, a small broad peak at ~800 °C suggests the reduction of Sn oxide far away from Ni center, possibly due to the activated H_2 spillover from the Ni sites, which thus occurs at a lower temperature than that of Sn/SiO_2. For $NiSn_{0.9}$ sample with higher Sn content, the reduction of NiO is still inhibited (with the reduction peak at 350 °C) as compared to monometallic Ni. While the disappearance of reduction peaks at much higher temperature (> 500 °C) in $NiSn_{0.9}$, as well as the slight shift the co-reduction of Ni and Sn oxide to lower reduction temperature (at 415 °C) as compared to that of $NiSn_{0.4}$, are possibly due to the closer interaction between Ni and Sn species at higher Sn content level (Fig. S2).

Quantification of the TPR results at < 550 °C range (Table S1) shows that the molar ratio of H_2 consumption to Ni (H_2/Ni) in pure Ni catalyst is 0.92, indicative of almost fully reduction of NiO. When assuming a same H_2/Ni ratio for Ni in the bimetallic NiSn samples, the excess H_2 could reduce ~56 % SnO_2 to Sn in $NiSn_{0.4}$ and ~80 % in $NiSn_{0.9}$, respectively. In this case, a metallic Sn/Ni molar ratio is estimated to be 0.26 and 0.70 for $NiSn_{0.4}$ and $NiSn_{0.9}$, respectively. It further confirms a concomitant reduction of Ni and Sn oxides at a low temperature (< 550 °C), indicative of a thermodynamically favorable interaction between the reduced Ni and the Sn oxide, which promotes the reduction of Sn oxide that are supposed to strongly interact with SiO_2 support. In addition, these results are consistent with the partial reduction of Sn to a metallic state.

As expected, after reduction at 400 °C in pure H_2 for 1 h, the XRD patterns (Fig. 1 C) only detects metallic Ni diffractions (PDF#04-0850) for monometallic Ni, while no Sn related diffractions for pure Sn catalyst, indicating of an absence of Sn agglomerates (Fig. S3). Notably, the bimetallic $NiSn_{0.9}$ presents distinct and intense diffraction peaks of well-identified Ni_3Sn_2 intermetallic phase (PDF#06-0414), with the unit cell structure shown in Fig. S4. However, $NiSn_{0.4}$ presents a wide diffraction peak at 42.8°, which has a distinct shift to lower angle as compared with the monometallic Ni (44.4°), clearly demonstrating the lattice expansion of the unit cell caused by the formation of a NiSn alloy. In fact, this peak can be attributed to the dominating diffraction peak of a new cubic Ni_3Sn intermetallic phase (PDF#65-9459, Fig. S4), in good agreement

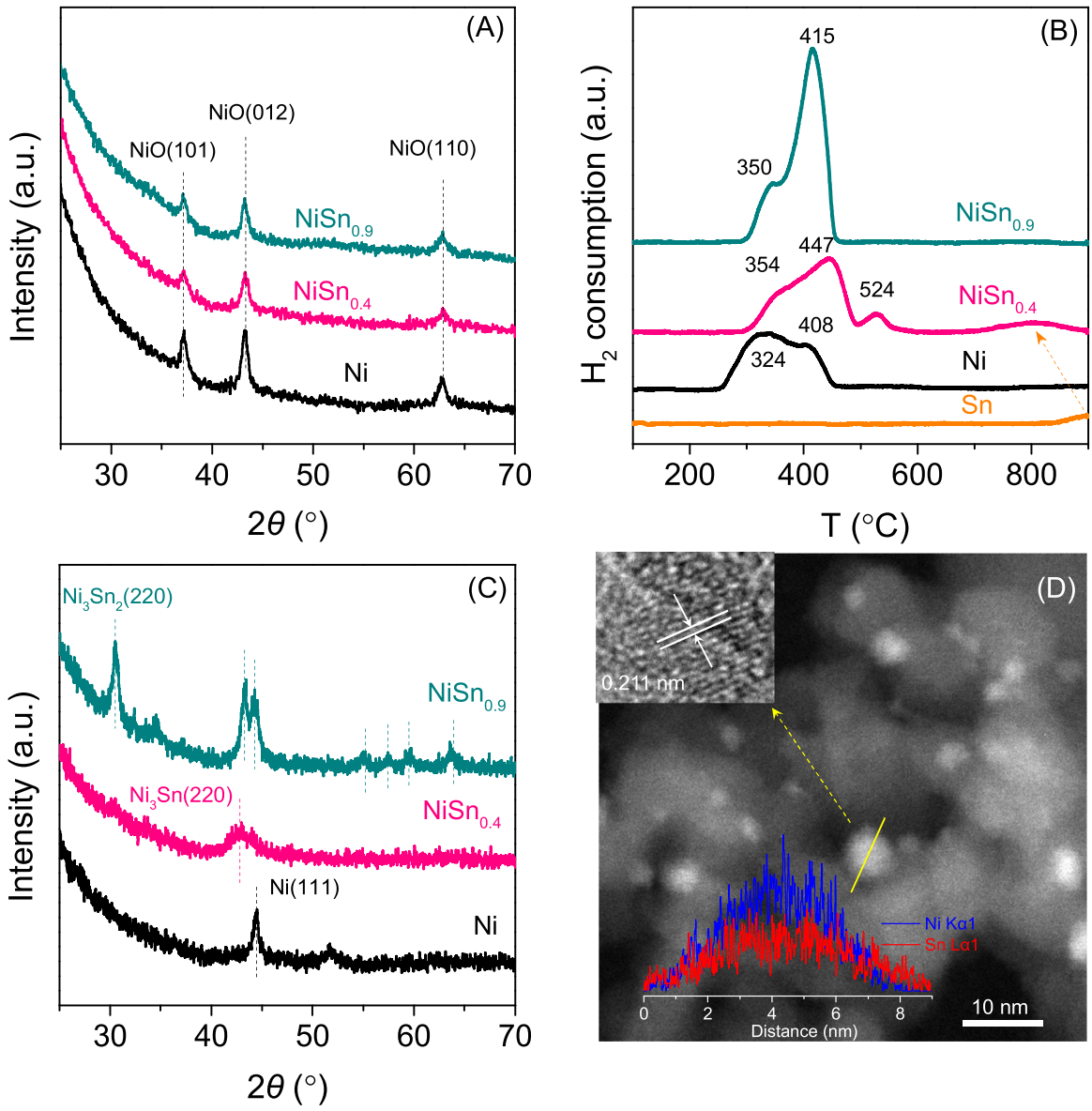

Fig. 1. (A) XRD patterns of catalysts after calcinations; (B) H_2-TPR profile of different catalysts; (C) XRD patterns of catalysts after reduction at 400 °C for 1 h; (D) HAADF-STEM image of $NiSn_{0.4}$ after ex-situ reduction, the inset images show the HRTEM and line scanning of a certain particle, respectively.

with previous reports [31,32]. The average particle size is estimated to be 3.0 nm for $NiSn_{0.4}$, significantly smaller than that of 11.4 nm for Ni, and 10.9 nm for $NiSn_{0.9}$. Nevertheless, the broad diffraction peak in $NiSn_{0.4}$ makes precise determination of the nanoparticle size and morphology of Ni_3Sn less certain.

High-angle annular dark field scanning transmission electron microscopy (HAADF-STEM), accompanied by energy dispersive spectroscopy (EDS) analysis was further performed on the reduced $NiSn_{0.4}$ nanoparticle to gain more information about the interaction between Ni and Sn. First of all, a number-weighted particle size of 4.1 ± 0.7 nm was obtained according to the STEM images (Fig. S5), which is close to the particle size estimated from XRD. EDS Mapping (Fig. S6) demonstrates the overlap of Ni and Sn elements on the same locations, consistent to the formation of NiSn alloy. Line scanning further conforms the intimate interaction between Sn and Ni throughout a particle's profile (Fig. 1D). In addition, HRTEM examines a lattice fringe of 0.211 nm for the particles in $NiSn_{0.4}$, corresponding well to the $Ni_3Sn(220)$ spacings in XRD, which further evidences the formation of the Ni_3Sn intermetallic structure.

The electronic and geometric structure of Ni and Sn in bimetallic catalysts after in situ reduction at 400 °C were explored by X-ray absorption structure (XAS) spectra. The normalized Ni K-edge X-ray absorption near edge structure (XANES) spectra of Ni, $NiSn_{0.4}$, and $NiSn_{0.9}$ suggests that Ni has been fully reduced to Ni metal (Fig. 2 A), consistent with XRD. However, the absorption edge of the two bimetallic NiSn samples moves to a lower photon energy, as compared to the reference monometallic Ni and Ni foil, implying a possible enhanced electronegativity of the Ni atoms [39], possibly derived from a second scattering atom within the bonding distance, i.e., metallic Sn atoms. Moreover, their low energy extended X-ray absorption fine structure (EXAFS) oscillations (as indicated in green region) are out of phase compared to monometallic Ni, which suggests modifications in the structural environment of Ni in the bimetallic samples. The EXAFS was transformed using k2 weighted Fourier transformed to determine the coordination number (CN) and bond distances of Ni-M bonds (Fig. 2B). In comparison with the monometallic Ni, the NiSn catalysts show a significant decrease in intensity of the Ni-M (e.g., Ni-Ni + Ni-Sn) scattering features in relation to the first nearest-neighbor distance between 1.7 and 2.8 Å (phase uncorrected distance), indicating a reduced Ni-M CN. Moreover, no scattering paths appear in the second shell (as indicated in yellow

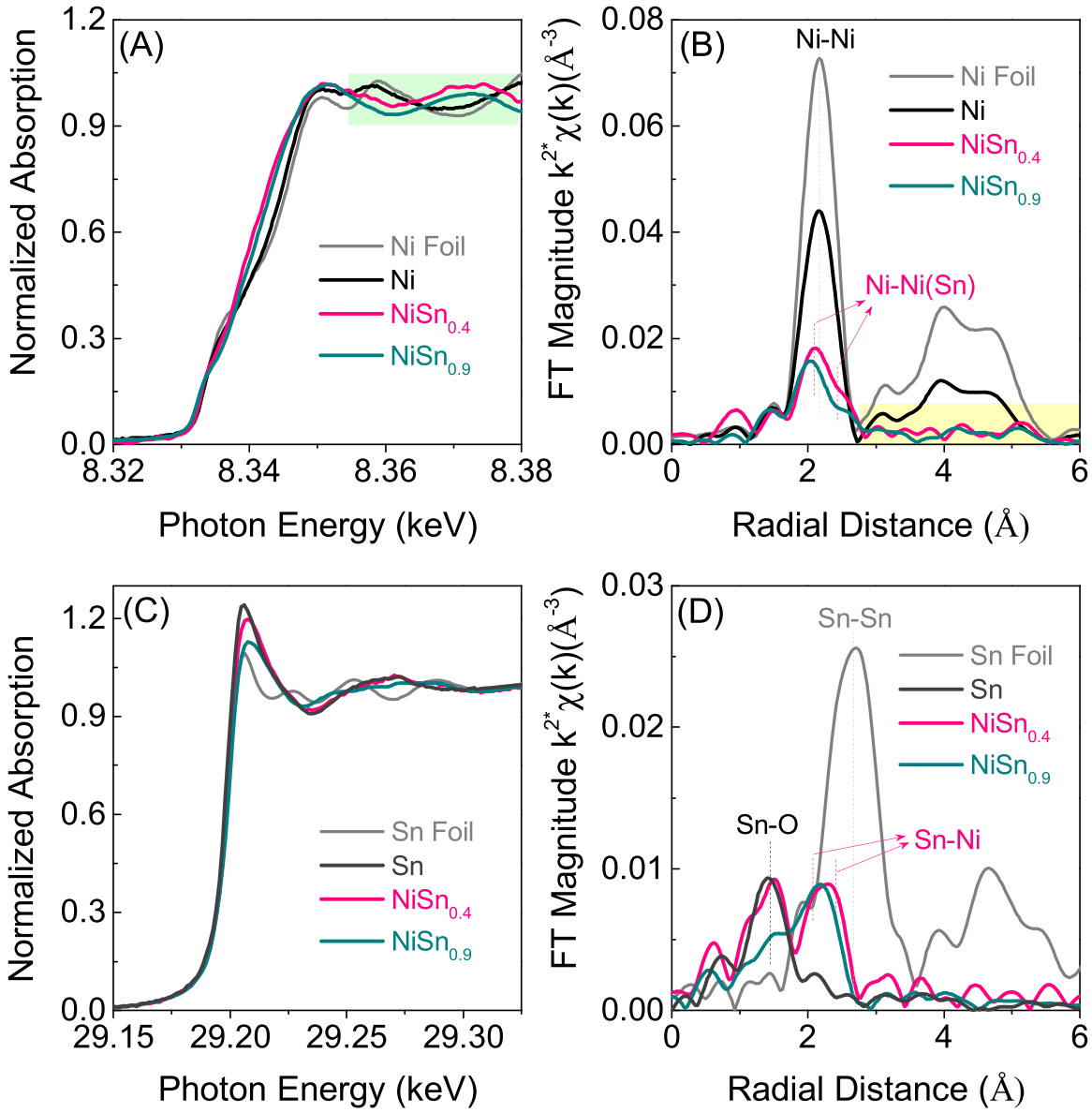

Fig. 2. (A) Normalized XANES at the Ni K edge; (B) Ni magnitude of Fourier transform of the k^2-weighted EXAFS spectra; (C) Normalized XANES at the Sn K edge; (D) Sn magnitude of the Fourier transform of the k^2-weighted EXAFS spectra. The catalysts were in situ reduced at 400 °C for XAS measurement.

region) for the bimetallic catalysts, indicating highly dispersed Ni sites in the NiSn intermetallics. Clearly, except for the Ni-Ni peak, a new bond distance emerges in bimetallic NiSn samples. Fits of the EXAFS data were obtained using two scattering paths, Ni-Ni or Ni-Sn [39]. It reveals the Ni-Ni CN of 8.7, 3.0 and 2.9 for Ni, with an additional Ni-Sn CN of 1.1 and 1.4 for $NiSn_{0.4}$ and $NiSn_{0.9}$, respectively (Table S2). The Ni-Ni bond length of NiSn samples (2.52 Å) is slightly larger than that of pure Ni, demonstrating a reduced Ni-Ni bond strength via the isolation effect of Sn. In addition, to further confirm the Ni_3Sn intermetallic phase in $NiSn_{0.4}$, we have also used the Ni_3Sn unit cell structure (Fig. S4) with two types of Ni-Ni bonds (2.58 and 2.99 Å) and Ni-Sn bonds (2.58 and 2.99 Å), predicted from XRD, as a reference to fit the spectra, interestingly, good fitting can be obtained (Table S3). It further evidences the formation of Ni_3Sn intermetallic for $NiSn_{0.4}$ catalyst.

To develop a complete understanding on both metals in $NiSn_{0.4}$ and $NiSn_{0.9}$, the Sn K edge was also measured by XANES (Fig. 2 C). The white line intensity decreases continuously from monometallic Sn/SiO_2 to $NiSn_{0.4}$ and further to $NiSn_{0.9}$, with increasing Sn content, suggesting that more Sn oxides participate in the formation of intermetallic species, in good agreement with TPR. Accordingly, the Sn K-edge EXAFS displays only Sn-O scattering path for monometallic Sn, but Sn-O and Sn-Ni for the bimetallic NiSn samples. Note there is no Sn-Sn bond in NiSn samples, indicating that the metallic Sn atoms are isolated by Ni, which is consistent to the formation of NiSn intermetallic phases (Ni_3Sn and Ni_3Sn_2). Quantification fitting with Sn-O and one type of Sn-Ni derives the Sn-O CN of 2.4, 1.3 and 0.5 for Sn, $NiSn_{0.4}$ and $NiSn_{0.9}$, respectively, as well as the Sn-Ni CN of 2.2 and 2.6 for $NiSn_{0.4}$ and $NiSn_{0.9}$, respectively (Table S2). In addition, if we also use the Ni_3Sn unit cell model to re-fit the Sn-Ni scattering path in $NiSn_{0.4}$, good fitting can also be obtained (Table S3), proving again the formation of Ni_3Sn.

X-ray photoelectron spectroscopy (XPS) was performed to analyze the electronic interaction between Ni and Sn. Note that due to the limitations of the instrument, the samples were ex-situ reduced, which may result in partial oxidation of the surfaces (Table S4). Fig. 3A displays the Ni 2p spectra with a deconvolution by Gaussian peak fitting. In order to better analyze the electronic modification, the spectral analysis was performed by fixing the Binding Energy (BE) of Ni^{2+} $2p_{3/2}$ and its satellite peak at 855.8 and 860.4 eV, respectively. Notably, the BE of Ni^0

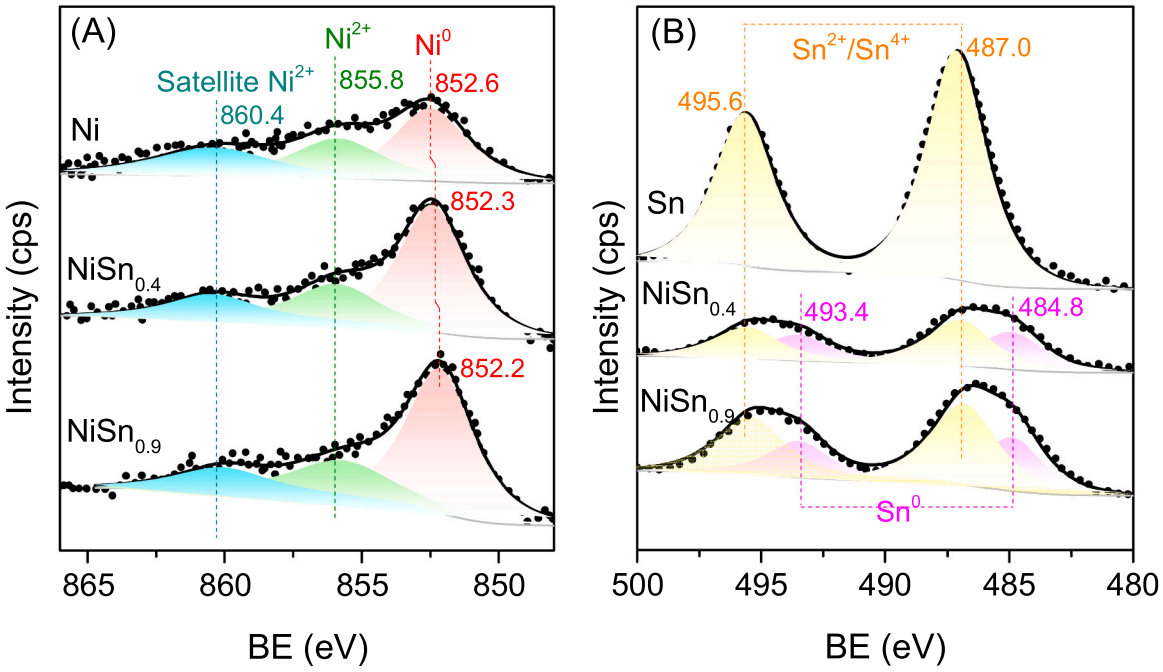

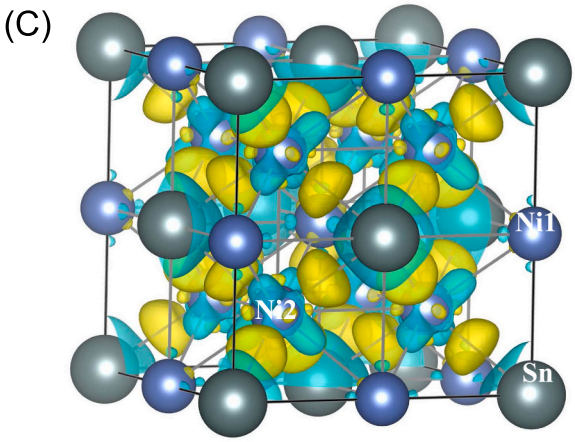

Bader charge	|e|
Ni1	-0.05
Ni2	-0.20
Sn	0.45

Fig. 3. XPS spectra of Ni 2p (A) and Sn 3d (B) for different catalysts. Dots are the experimental data, while the line and area are fitting results. The catalysts were ex-situ reduced at 400 °C. (C) Bader and deformation charge density distribution for the Ni and Sn atoms in a Ni_3Sn unit, yellow and blue regions represent increasing and decreasing electron densities, respectively; where the table shows the electron changes for two typical Ni atoms and a Sn atom as labeled.

shifts from 852.6 eV (monometallic Ni) to 852.3 eV ($NiSn_{0.4}$) and further to 852.2 eV ($NiSn_{0.9}$). These clear shifts to lower BE with increasing Sn content can be assigned to the electron transfer from Sn to Ni, owning to the formation of NiSn intermetallic [32,39,40]. The Sn 3d XPS spectra (Fig. 3B) records of both Sn^0 and Sn^{4+} in bimetallic NiSn [41], but only Sn^{4+} for the monometallic Sn, in accordance with above TPR and XAS. In order to further understand the electronic interactions between Ni and Sn, the Bader and deformation charge density distribution for Ni and Sn atoms in a Ni_3Sn unit was calculated by DFT. As shown in Fig. 3C, a strong redistribution of electronic charges can be observed around the Ni and Sn atoms, showing electron transfer from Sn to Ni. The charge quantity of Ni atom has enhanced 0.05 or 0.2 |e|, respectively, depending on the number of adjacent Sn atoms, while that of Sn atom has decreased 0.45 |e|. Notably, the direction of these electronic interaction between Ni and Sn is contrary to that of other oxophilic metal-Ni bimetallic alloy phases, such as NiRe [42], NiW [43], NiFe [18] et al., in which the observed electron transfer was from Ni to the oxophilic metals. It appears a unique role of Sn in modifying the chemical properties of Ni, which also imply that the Sn here may not play the role of an oxophilic promoter to stabilize O functional groups in biomass derived furans or phenols [44].

3.2. Surface chemistry of bimetallic NiSn/SiO_2 catalysts

To explore the surface geometry and chemical properties of Ni sites by the presence of Sn, in situ CO adsorption DRIFTS was performed (Fig. 4 A). As expected, CO adsorbs on monometallic Ni both in the linear (at the vibrational frequencies of 2084 and 2050 cm^{-1}) and bridge forms (1940 cm^{-1}). These frequencies can be ascribed to CO adsorbed on metallic Ni ensembles with a mixture of low- and high-coordination sites [45–47]. However, the adsorption of CO on Sn site is undetectable at ambient temperature. For $NiSn_{0.4}$ and $NiSn_{0.9}$, the bridge-coordinated CO was absent, instead, only a linear adsorption of CO was observed, indicative of the absence of Ni ensembles in NiSn intermetallic (Ni_3Sn or Ni_3Sn_2) structures [27]. Moreover, red shift of the linear adsorption occurs from monometallic Ni (2084 cm^{-1}) to Ni_3Sn (2075 cm^{-1}) [32] and further to Ni_3Sn_2 (2061 cm^{-1}). In accordance with the XPS measurement for the electron transfer from Sn to Ni, the increased electron density of Ni enhances electron feedback from *d* orbital of Ni to π * orbital of CO, and therefore the Ni-C bond is strengthened while the C-O bond is weakened, resulting in a red shift in the C-O stretching frequency [47–49].

The changes in heat of adsorption of CO on NiSn intermetallic

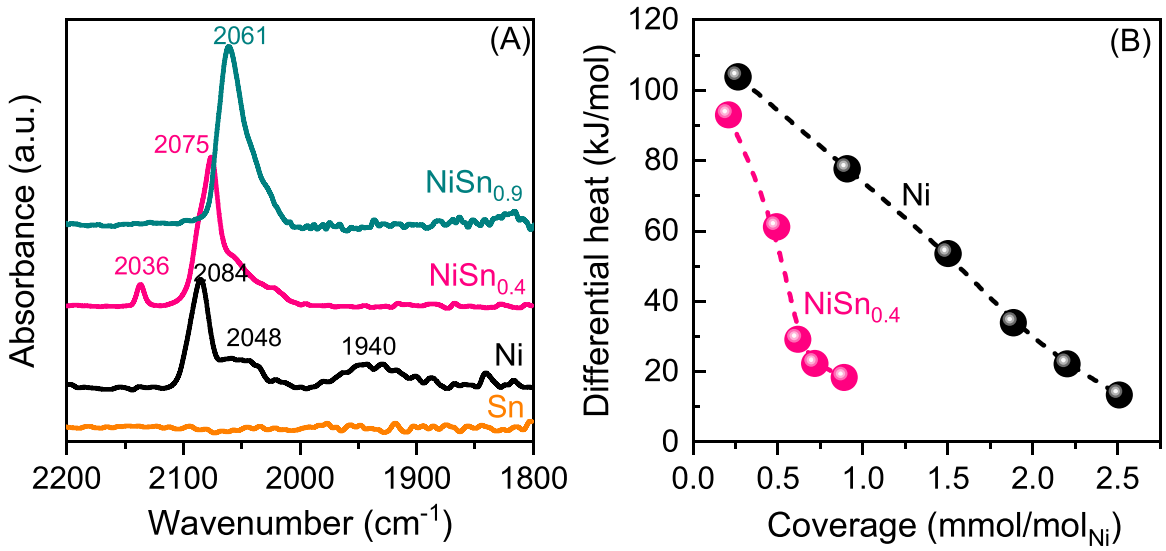

Fig. 4. (A) DRIFTS spectra of CO adsorption at 20 °C; (B) Microcalorimetric measurement of CO chemisorption. The catalysts were in-situ reduced at 400 °C.

surfaces is also evident from CO microcalorimetry. As shown in Fig. 4B, the amounts of CO adsorbed in each case were estimated to be 1.75 and 0.59 $mmol_{CO}/mol_{Ni}$ for Ni and $NiSn_{0.4}$, respectively, demonstrating that the formation of Ni_3Sn with a Sn-enriched surface leads to decreased number of Ni adsorption sites despite the smaller nanoparticle size. In addition, the initial heats of adsorption for CO were determined to be 104.5 and 92.6 kJ/mol for Ni and $NiSn_{0.4}$, respectively, in good agreement with a previous study of CO adsorption on Ni and Ni_3Sn surface [50].

Due to the relevance in hydrogenation and hydrogenolysis reactions, the H-H bond dissociation activity was investigated on Ni and bimetallic NiSn catalysts, using the H_2/D_2 exchange reaction. As shown in the H_2-D_2-TPSR profiles (Fig. 5), the evolution of exchanged HD product starts at around ~30 °C over Ni, ~50 °C on Ni_3Sn ($NiSn_{0.4}$), and ~100 °C on Ni_3Sn_2 ($NiSn_{0.9}$). Moreover, HD product quickly reaches equilibrium at ~120 °C on Ni, but requires higher temperature of ~170 °C on Ni_3Sn, and much higher temperature of > 200 °C on Ni_3Sn_2. These results indicate significant inhibition of H_2 dissociation in presence of Sn, especially in the case of more Sn-rich surfaces. In addition, the semi-quantitative H_2 dissociation rate at a constant temperature of 70 °C was also measured (Fig. S7). Ni shows ~2.5 and ~11 times higher activity than the Ni_3Sn and Ni_3Sn_2, respectively. Previous studies have suggested that the Sn atoms induce a charge transfer with other metal atoms, such as Pt, Pd and Ni, leading to a lower rates of H-H dissociation and hydrogenation reactions [30,51]. It is expected, therefore, that for the NiSn intermetallic catalysts, inhibition of H_2 dissociation may lead to reduced hydrogenation and hydrogenolysis activity during HDO of furfural (FAL).

3.3. *Furfural and furfuryl alcohol adsorption on Ni(111) and Ni_3Sn (110) surfaces*

DFT calculations were then carried out to investigate the FAL adsorption geometry and stability on the Ni_3Sn intermetallic active phase. On the basis of above characterizations, the most exposed Ni_3Sn (110) surface (i.e., the Ni_3Sn(220) diffraction in XRD) with a surface Ni/Sn ratio of 1:1 was selected as the calculation model. For comparison, the Ni(111) surface was taken as the model for the Ni/SiO_2 catalyst with a high density of Ni ensembles. Four types of adsorption structures, including cis/trans-parallel and cis/trans-vertical adsorption mode were examined (see Fig. S8). In the case of pure Ni(111), the most stable configuration was the cis-parallel adsorption mode with the C═O bond in carbonyl group bridge-adsorbed on the top site of Ni, and the furan

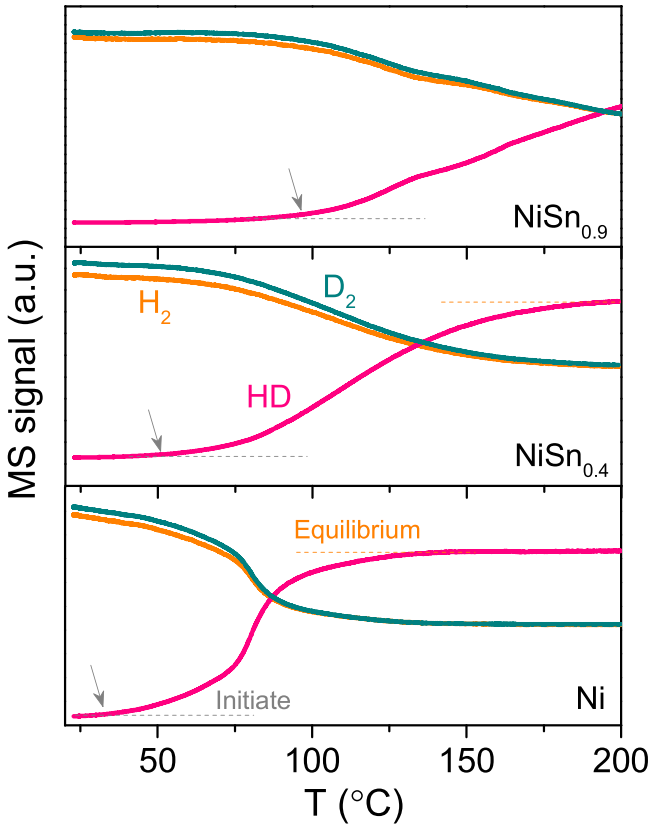

Fig. 5. Profiles of H_2, D_2 and HD evolution during H_2-D_2-temperature programed surface reaction from room temperature to 200 °C.

adsorbed parallel on the surface across two 3-fold hollow sites, which shows a high adsorption energy of − 1.88 eV (Fig. 6A) [18,39]. However, in Ni_3Sn(110) surface, the Sn atom itself is repulsion for both O and C atoms in FAL, consistent with previous reports on CO_2 adsorption on NiSn alloy [44], but in stark contrast to the behavior of other will-identified oxophilic metals like Fe, Cu or Mo, which favors O bonding [18,26,27]. Instead, the Ni_3Sn(110) surface allows a tilted adsorption configuration (trans-vertical mode) through the carbonyl O of FAL bonding on the top of isolated Ni atom, with the Ni-O bond

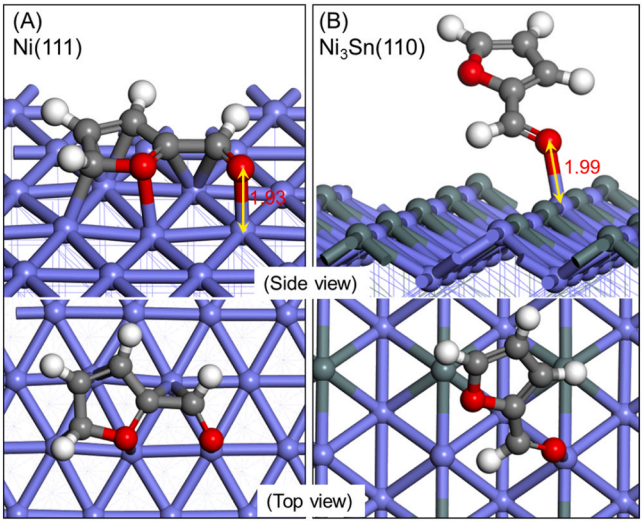

Fig. 6. The most stable configuration of Furfural adsorption on (A) Ni(111) and (B) $Ni_3Sn(110)$ surface, respectively. The Ni, Sn, O, H and C atoms are in blue, cyan, red, white and gray, respectively. The unit of distance is Å.

distance of 1.99 Å, and a relative strong adsorption energy of − 0.79 eV (Fig. 6B). Bader charge analysis suggests a distinct electron transfer from Ni to the adsorbed carbonyl O. It therefore infers that the electronic interaction between Sn and Ni promotes the adsorption of carbonyl on the isolated Ni atom.

It is likely that the tilted adsorption mode of FAL on the NiSn intermetallic limits the furan ring surface interaction and suppresses the rates of the furan ring reactions, e.g., ring hydrogenation and hydrogenolysis; while, the enhanced adsorption of the carbonyl group may lead to selective conversion of furfural to more valued furfuryl alcohol (FOL) [39], and even 2-methylfuran (MF).

3.4. Furfural conversion

Fig. 7 A shows FAL conversion and product distribution as a function of space time over monometallic Ni catalyst at 250 °C and 1 atm H_2 pressure. The initial major product is furan along with CH_4, derived from the decarbonylation reaction. As conversion increase, the furan undergoes C-C hydrogenolysis and ring opening to CH_4 and C4 (including butanal, butanol and butane), which are typical reactions on pure Ni active sites [18]. There is also minimal selectivity to furfuryl alcohol (FOL), tetrahydrofurfuryl alcohol (HFOL), resulting from hydrogenation of furan ring and/or carbonyl group hydrogenation. While FOL can be further deoxygenated to 2-methylfuran (MF), the highest MF yield over the whole conversion process reaches only 4.5 %, demonstrating a poor performance of Ni ensemble for MF production. The reaction network of FAL conversion is summarized in Fig. 7B.

Unlike monometallic Ni, the side reactions of decarbonylation, hydrogenolysis and ring opening, which produce furan, CH_4 and C_4 products, have been eliminated on the NiSn intermetallic catalysts. As seen in Fig. 7C, at conversion level of ~20 %, the dominant product changes to MF, with a selectivity of 60 % or 65 % on Ni_3Sn or Ni_3Sn_2 catalyst, respectively. Additional products include FOL as well as a minor amount of C5 products from ring opening of FOL. While the MF selectivity on NiSn intermetallic catalysts is significantly improved, the FAL conversion rate is lower than that of monometallic Ni. For example, the rate of Ni is ~2.3 and ~8.0 times higher than that of Ni_3Sn and Ni_3Sn_2, respectively. This is in part because of the different reaction paths, but may also be due to the decreased H_2 dissociation activity as suggested by H_2-D_2-TPSR. Although the FAL conversion rate is lower, the MF formation rate on the Ni_3Sn and Ni_3Sn_2 are higher, e.g., ~4.0 and ~1.3 times higher than that of Ni. These results suggest that the isolated Ni sites in intermetallic limit the furan ring chemistry, while also allow a considerable activity toward target MF, especially for Ni_3Sn.

To further confirm that there are no other side reactions at any conversion level on Ni_3Sn, Fig. 7D presents the product evolution for FAL conversion as a function of W/F. Clearly, FOL and MF are the two initial products, while as the extent of reaction progresses, FOL was finally converted to MF and a small amount of C5, demonstrating that FOL is the intermediate to MF, consistent with previous reports studies [18,22,26]. A more intuitive comparsion between Ni and $NiSn_{0.4}$ catalyst for the activity and product selectivities are shown in Fig. S9, which further stands out the unique role of Sn in tuning selectivity. Moreover, the MF selectivity is clearly higher than that of $NiFe/SiO_2$ (~39 %) and $PdFe/SiO_2$ (~63 %) bimetallic catalysts performed at same reaction conditions and same conversion level of ~100 %, which is also comparable to that of the optimized NiCu or NiMo based catalysts performed at liquid phase using solvent (Table S5).

To shed more light on the results obtained with FAL reaction, the intermediate FOL conversion was also conducted on Ni and $NiSn_{0.4}$ catalysts. Fig. 8 compares the conversion and product distributions from the reaction of FAL and FOL at same reaction conditions. Unlike the FAL reaction, the MF yield was dramatically higher from FOL conversion on both Ni and $NiSn_{0.4}$, suggesting that FOL is an intermediate for the consecutive reaction of FAL to MF. With monometallic Ni, there are still side reactions from furan ring chemistry for FOL conversion, including furan, C4 and CH_4, at both low and high conversions by varying W/F, similar to the reaction of FAL. For $NiSn_{0.4}$, however, the major product was MF, with one minor product of FAL from FOL dehydrogenation, again supporting the importance of isolated Ni sites in limiting furan ring chemistry.

Notably, for FOL reaction, the rate on $NiSn_{0.4}$ is slightly higher than that on monometallic Ni, which differs from the FAL reaction. This comparison demonstrates that the decreased hydrogenation activity of $NiSn_{0.4}$ in the FAL reaction originates from its lower activity in the first step of FAL hydrogenation to FOL, which could be ascribed to the distinct inhibition in H_2 dissociation activity at atmosphere pressure. As expected, increasing the H_2 pressure to 2 MPa largely accelerates the hydrogenation rates even on Ni_3Sn_2, which shows a facile barrier for hydrogenation of carbonyl in FAL on the isolated Ni sites in Ni_3Sn_2 according to DFT calculations [39].

To corroborate these experimental measurements, DFT calculations were performed to examine the dissociative adsorption of H_2, as well as FAL hydrogenation followed by deoxygenation over the $Ni_3Sn(110)$ surface at the reaction temperature of 250 °C, respectively. In agreement with the H_2-D_2-TPSR results, the H_2 dissociation energy on $Ni_3Sn(110)$ surface (0.24 eV) is higher than that on Ni(111) surface (0.07 eV), as the H-H bond requires to be elongated longer (1.54 vs. 1.13 eV) to reach the transition state of H_2 dissociation due to geometric effect of Sn (Fig. S10). While the hydrogenation of FAL to FOL contains two elementary steps with the H atoms added to the C and O in the carbonyl group sequentially, with the highest energy barrier of 1.14 eV (Fig. S11).

To further understand the deoxygenation of intermediate FOL on Ni_3Sn, DFT calculations were performed for FOL adsorption and C-OH cleavage on $Ni_3Sn(110)$ surface (Fig. 9A). Similar to the adsorption configuration of FAL on $Ni_3Sn(110)$ surface, FOL also favors a vertical adsorption mode on the isolated Ni atom through its hydroxy O sitting on top of the isolated Ni atom, with a Ni-O bond distance of 2.11 Å, and an adsorption energy of − 0.65 eV. In addition, the C-OH bond has been lengthened to 1.46 Å, as compared to 1.41 Å in gas phase FOL, indicative of activation of C-OH bond. From the initial state (IS) of this most stable configuration, the C-OH goes breaking with both the -OH and furan-CH_3* fragments binding at the same Ni atom in the transition state (TS), which shows an energy barrier of 0.80 eV. In the final state (FS), the furan-CH_3* remains on the initial Ni atom, while the O* moves onto a Ni-Ni bridge site. Notes that this activation barrier for C-OH cleavage is slightly lower than the carbonyl hydrogenation step (1.14 eV), demonstrating the hydrogenation step might be the rate determining step

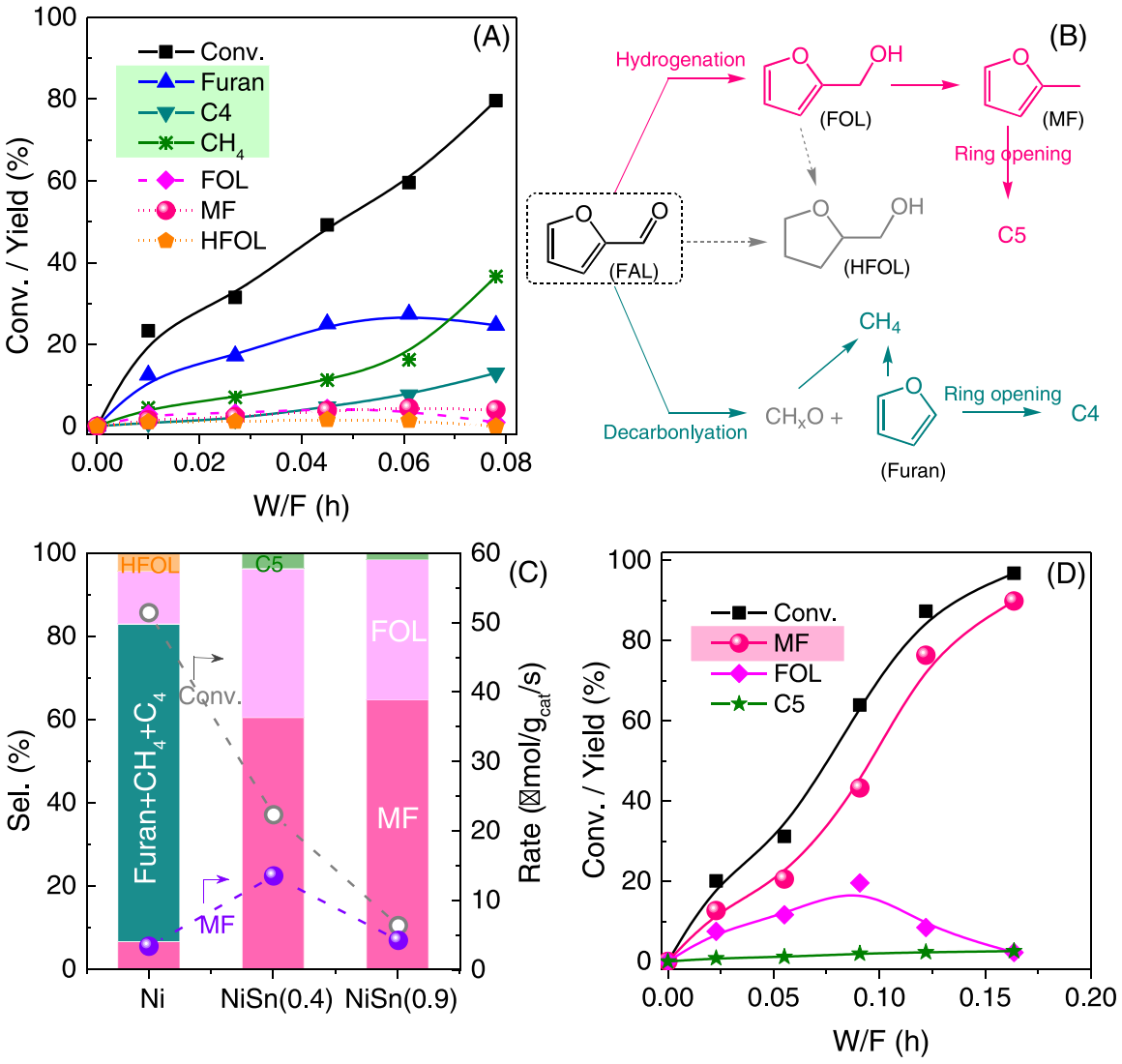

Fig. 7. (A) Furfural (FAL) conversion and product distributions as a function of W/F over Ni catalyst; (B) Reaction network for FAL conversion; (C) Product selectivity over different catalysts at 21 ± 2 % FAL conversion level by adjusting W/F, as well as the initial reaction rate for FAL conversion and 2-methylfuran (MF) formation estimated at FAL conversion lower than 23 %; (D) FAL conversion and product distributions as a function of W/F over $NiSn_{0.4}$ catalyst; $NiSn/SiO_2$, respectively. Reaction conditions: T = 250 °C, P = 1 atm, TOS = 30 min.

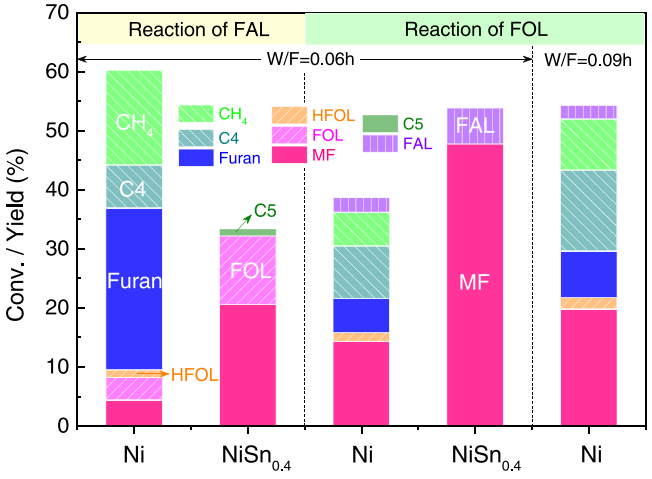

Fig. 8. Furfural (FAL) and Furfuryl alcohol (FOL) conversion and product distributions over Ni and $NiSn_{0.4}$ catalysts, respectively. Reaction conditions: T = 250 °C, P = 1 atm, TOS = 30 min.

during the sequential reactions of FAL to MF (Fig. S11). To demonstrate the efficiency of the Ni_3Sn active phase in C-OH scission, the deoxygenation of FOL on Ni(111) surface has also been studied for comparison, as shown in Fig. 9B. In the IS state, FOL prefers a parallel adsorption configuration with the four C in furan ring and the hydroxyl O bonding to Ni sites, leading a strong adsorption energy of − 1.84 eV. Notably, a slightly longer Ni-O bond of 2.19 Å and a shorter C-OH bond of 1.43 Å were observed on Ni(111), as compared to those on $Ni_3Sn(110)$ surface, demonstrating a weaker activation of C-OH bond in Ni(111). Followed, in the TS of C-OH cleavage, the adsorbed FOL transforms to -OH and furan-CH_3* fragments, with an energy barrier of 1.03 eV, which is even higher than that over $Ni_3Sn(110)$. The results suggest that the isolated Ni site in $Ni_3Sn(110)$ is even more facile for FOL deoxygenation to MF than that of the basal plane of Ni(111), which is in good agreement with the reaction results for FOL conversion. In addition, besides the energy demanding deoxygenation path, the paralleled adsorption mode of both FAL and FOL on Ni(111) surface offers other more energetic favorable reaction paths, such as hydrogenation and decarbonylation on the Ni sites, thus leading to poor MF selectivity on monometallic Ni catalyst.

Despite the activity and selectivity, stability is also an important issue in evaluating the catalysts. Fig. 10 A further compares the stability

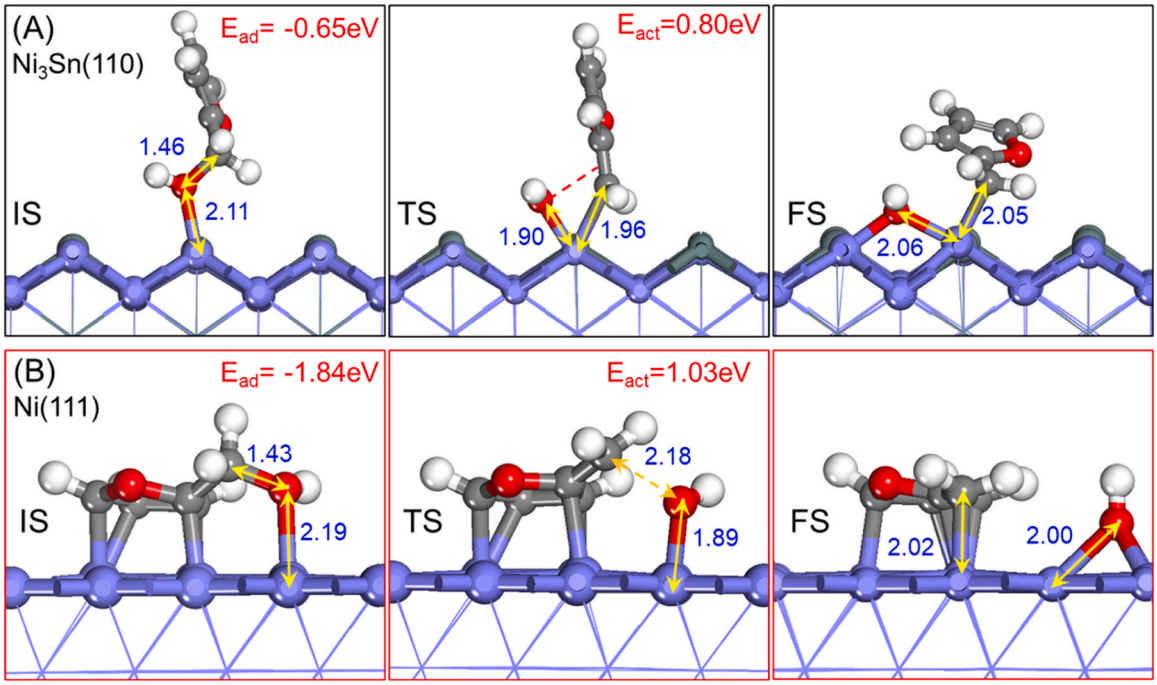

Fig. 9. Side view of structures of initial state (IS), transition state (TS), and final state (FS) for C-OH cleavage of FOL on (A) $Ni_3Sn(110)$ and (B) Ni(111) surface, respectively. The Ni, Sn, O, H and C atoms are in blue, cyan, red, white and gray, respectively. The unit of distance is Å.

of Ni and $NiSn_{0.4}$ during HDO of FAL. The space time was adjusted to obtain similar initial conversion of 87–96 %, which was controlled to be lower than 100 %. Interestingly, the $NiSn_{0.4}$ is much more stable than that of the monometallic Ni, indicative of the appealing role of Sn in enhancing stability. The deactivation of the catalysts is related to either the sintering of the active phase or the deposition of carbon that blocks the active sites. Since XRD patterns record identical diffractions peaks on the spent Ni or $NiSn_{0.4}$, as compared to that of the fresh catalyst, respectively (Fig. S12), it demonstrates that sintering is not significant under current mild reaction conditions. What's more, when changing the conversion level by either deactivating catalyst or varying space time over both catalysts (Fig. 10B and C), the yields of the major products fall near the same trend line as a function of FAL conversion. This comparison indicates that deactivation of catalysts reduces the numbers of active sites without altering the reaction chemistry, as a result, coke should be the major reason for deactivation [52]. TPO of spent catalysts was then performed to quantify the coke formation during HDO of FAL. As shown in Fig. 10D, the monometallic Ni catalyst presents a major CO_2 evolution peak at 333 °C, with small peaks at 365 and 529 °C. In contrast, the $NiSn_{0.4}$ presents broad peaks between 315 and 447 °C. Such difference in coke oxidation temperature demonstrates different types of carbon deposition [53]. Generally, the low temperature peak (< 500 °C) is related to hydrogen rich carbon, which might be due to the oligomers deposition from FAL and/or products; while the high temperature (> 500 °C) is assigned to hydrogen deficient graphite-like carbon, possibly derived from C-C hydrogenolysis side reaction which only occurs on monometallic Ni catalyst. In addition, the quantified amount of carbon is 2.32 % and 0.49 % $g_{carbon}/g_{catalyst}$ on Ni and $NiSn_{0.4}$, respectively, which is consistent with the stability of the catalysts. The above analysis clearly points that the presence of Sn reduces carbon deposition during HDO of FAL, and therefore enhances the stability of the catalyst. Similar phenomenon has been observed in reforming or dehydrogenation reactions, in which Sn alloying with Ni was found to have a positive effect towards increased stability through inhibition of carbon nucleation on the Ni sites [41,54]. It has been suggested that the Sn atom has a similar electronic structure to C, which favors the interaction of Sn p orbitals with Ni 3d electrons, thereby reducing the chance of nickel carbide formation as a coke precursor [41, 54]. Note such role of Sn in preventing coking formation has not been reported on oxophilic promoter base bifunctional catalysts during HDO of biomass derived oxygenates, instead, the oxophilic center may accelerate deactivation [55,56], which again evidences the unique role of Sn in modulating selectivity and stability in HDO reactions.

4. Conclusion

In conclusion, this study shows that nano-sized Ni_3Sn intermetallic compound enables considerable activity and high selectivity toward target MF (91 % selectivity at 96 % conversion), with few side reaction products resulting from ring chemistry (decarbonylation, C-C hydrogenation and ring opening), which readily occurs with monometallic Ni catalysts. The formation of NiSn intermetallic compounds give surface structures with geometrically isolated Ni sites, along with electron transfer from Sn to Ni. A detailed experimental and theoretical investigations suggest that this electron modification of Sn to Ni increases carbonyl O bond strength in FAL to isolated Ni atoms, while the isolated Ni site prevents furan ring interaction. Such adsorption mode significantly reduces non-selective side reactions from ring hydrogenation. Moreover, it also allows a facile sequential reaction of carbonyl (C═O) hydrogenation followed by C-OH scission to generate 2-methylfuran. Although further Sn incorporation and formation of the Ni_3Sn_2 intermetallic structure still displays high MF selectivity, higher Sn surface coverage results in low FAL rates due to the strong inhibition in H_2 activation. In addition, the presence of Sn also significantly enhances the catalyst stability through inhibition carbon deposition on Ni sites.

CRediT authorship contribution statement

Feifei Yang: Conceptualization, Data curation, Formal analysis, Investigation, Writing - original draft. **Tianyu Zhang:** Supervision, Writing - review & editing. **Jiankang Zhao:** Software, Writing - review & editing. **Wei Zhou:** Supervision, Writing - review & editing. **Nicole J. Libretto:** XAS data curation, Writing - review & editing. **Jeffrey T. Miller:** XAS Resources, Writing - review & editing.

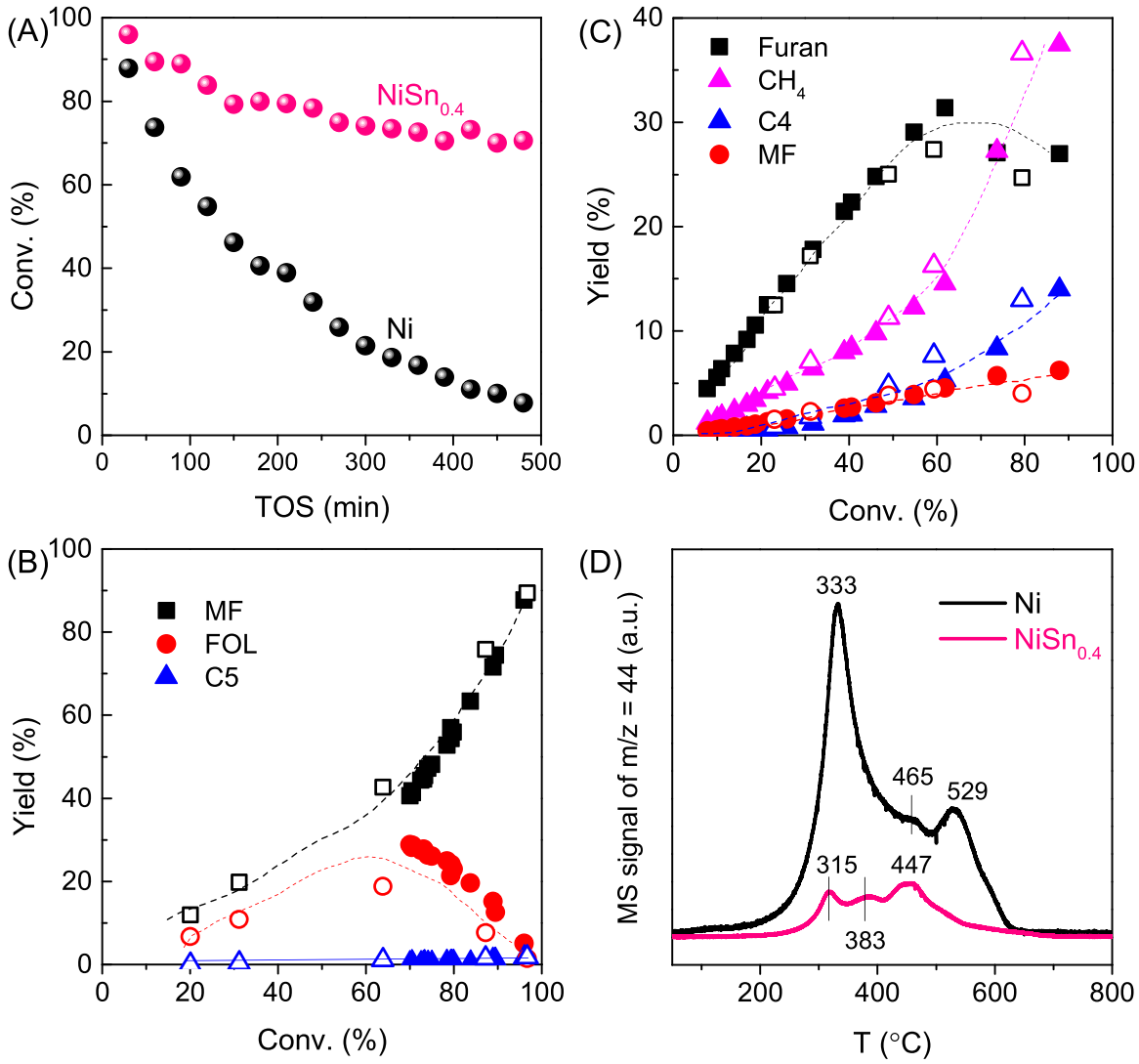

Fig. 10. (A) FAL conversion as a function of TOS on Ni and $NiSn_{0.4}$ at reaction conditions of W/F = 0.09 or 0.16 h for Ni or $NiSn_{0.4}$, P = 1 atm; Major Products yield as a function of FAL conversion on Ni (B) and $NiSn_{0.4}$ (C), the different FAL conversions were obtained by deactivating catalyst (solid symbols, from Fig. 10 A) and by adjusting W/F (open symbols, from Fig. 7A and D); (D) TPO profiles of spent Ni and $NiSn_{0.4}$ catalysts after HDO of FAL at same reaction conditions of W/F = 0.16 h, P = 1 atm, TOS = 500 min.

Declaration of Competing Interest

The authors declare that they have no known competing financial interests or personal relationships that could have appeared to influence the work reported in this paper.

Data availability

Data will be made available on request.

Acknowledgements

This research was funded by the Fundamental Research Funds for the Central Universities (2023QN1012 and 2021QN1046) in China, the 2021 Innovation and Entrepreneurship Doctor Program of Jiangsu Province (JSSCBS20211239), and the Open Sharing Fund for the Large-scale Instruments and Equipment of China University of Mining and Technology (CUMT). The XAS research used resources of 537 the Advanced Photon Source, a U.S. Department of Energy (DOE) Office of Science User Facility operated 538 for the DOE Office of Science by Argonne National Laboratory under Contract No. DE-AC02-06CH11357, and was supported by the National Science Foundation under Cooperative Agreement No. EEC-1647722 and National Science Foundation, Chemical, Engineering, Biological, and Transport Systems (CBET) Division, award 1804712. The authors deeply appreciate Prof. Daniel E. Resasco for the valuable suggestions.

Appendix A. Supporting information

Supplementary data associated with this article can be found in the online version at doi:10.1016/j.apcatb.2023.123176.

References

[1] E.L. Kunkes, D.A. Simonetti, R.M. West, J.C. Serrano-Ruiz, C.A. Gartner, J. A. Dumesic, Catalytic conversion of biomass to monofunctional hydrocarbons and targeted liquid-fuel classes, Science 322 (2008) 417–421.
[2] S. Chu, A. Majumdar, Opportunities and challenges for a sustainable energy future, Nature 488 (2012) 294–303.
[3] J.P. Lange, E. van der Heide, J. van Buijtenen, R. Price, Furfural-a promising platform for lignocellulosic biofuels, ChemSusChem 5 (2012) 150–166.
[4] K. Yan, G. Wu, T. Lafleur, C. Jarvis, Production, properties and catalytic hydrogenation of furfural to fuel additives and value-added chemicals, Renew. Sustain. Energy Rev. 38 (2014) 663–676.

[5] X. Li, P. Jia, T. Wang, Furfural: a promising platform compound for sustainable production of C4 and C5 chemicals, ACS Catal. 6 (2016) 7621–7640.
[6] S. Chen, R. Wojcieszak, F. Dumeignil, E. Marceau, S. Royer, How catalysts and experimental conditions determine the selective hydroconversion of furfural and 5-hydroxymethylfurfural, Chem. Rev. 118 (2018) 11023–11117.
[7] A.T. Hoang, V.V. Pham, 2-Methylfuran (MF) as a potential biofuel: a thorough review on the production pathway from biomass, combustion progress, and application in engines, Renew. Sustain. Energy Rev. 148 (2021), 111265.
[8] S. Wang, V. Vorotnikov, D.G. Vlachos, Coverage-induced conformational effects on activity and selectivity: hydrogenation and decarbonylation of furfural on Pd(111), ACS Catal. 5 (2014) 104–112.
[9] V.V. Pushkarev, N. Musselwhite, K. An, S. Alayoglu, G.A. Somorjai, High structure sensitivity of vapor-phase furfural decarbonylation/hydrogenation reaction network as a function of size and shape of Pt nanoparticles, Nano Lett. 12 (2012) 5196–5201.
[10] A.V. Mironenko, D.G. Vlachos, Conjugation-driven "Reverse Mars-van Krevelen"-type radical mechanism for low-temperature C-O bond activation, J. Am. Chem. Soc. 138 (2016) 8104–8113.
[11] Y. Deng, R. Gao, L. Lin, T. Liu, X.D. Wen, S. Wang, D. Ma, Solvent tunes the selectivity of hydrogenation reaction over alpha-MoC catalyst, J. Am. Chem. Soc. 140 (2018) 14481–14489.
[12] M.E. Witzke, A. Almithn, C.L. Conrad, M.D. Triezenberg, D.D. Hibbitts, D. W. Flaherty, In situ methods for identifying reactive surface intermediates during hydrogenolysis reactions: C-O bond cleavage on nanoparticles of nickel and nickel phosphides, J. Am. Chem. Soc. 141 (2019) 16671–16684.
[13] J. Zhang, B. Wang, E. Nikolla, J.W. Medlin, Directing reaction pathways through controlled reactant binding at Pd-TiO_2 interfaces, Angew. Chem. 56 (2017) 6594–6598.
[14] J. Fu, J. Lym, W. Zheng, K. Alexopoulos, A.V. Mironenko, N. Li, J.A. Boscoboinik, D. Su, R.T. Weber, D.G. Vlachos, C-O bond activation using ultralow loading of noble metal catalysts on moderately reducible oxides, Nat. Catal. 3 (2020) 446–453.
[15] K.A. Goulas, A.V. Mironenko, G.R. Jenness, T. Mazal, D.G. Vlachos, Fundamentals of C–O bond activation on metal oxide catalysts, Nat. Catal. 2 (2019) 269–276.
[16] S.H. Pang, C.A. Schoenbaum, D.K. Schwartz, J.W. Medlin, Effects of thiol modifiers on the kinetics of furfural hydrogenation over Pd catalysts, ACS Catal. 4 (2014) 3123–3131.
[17] D.M. Alonso, S.G. Wettstein, J.A. Dumesic, Bimetallic catalysts for upgrading of biomass to fuels and chemicals, Chem. Soc. Rev. 41 (2012) 8075–8098.
[18] S. Sitthisa, W. An, D.E. Resasco, Selective conversion of furfural to methylfuran over silica-supported NiFe bimetallic catalysts, J. Catal. 284 (2011) 90–101.
[19] Z. Jiang, W. Wan, Z. Lin, J. Xie, J.G. Chen, Understanding the role of M/Pt(111) (M = Fe, Co, Ni, Cu) bimetallic surfaces for selective hydrodeoxygenation of furfural, ACS Catal. 7 (2017) 5758–5765.
[20] D. Shi, J.M. Vohs, Deoxygenation of biomass-derived oxygenates: reaction of furfural on Zn-modified Pt(111), ACS Catal. 5 (2015) 2177–2183.
[21] S. Sitthisa, T. Pham, T. Prasomsri, T. Sooknoi, R.G. Mallinson, D.E. Resasco, Conversion of furfural and 2-methylpentanal on Pd/SiO_2 and Pd-Cu/SiO_2 catalysts, J. Catal. 280 (2011) 17–27.
[22] L. Chen, Y. Shi, C. Chen, H. Feng, S. Wang, X. Zhang, M. Wei, Precise control over local atomic structures in Ni-Mo bimetallic alloys for the hydrodeoxygenation reaction: a combination between density functional theory and microkinetic modeling, J. Phys. Chem. C 126 (2022) 4319–4328.
[23] O.F. Aldosari, S. Iqbal, P.J. Miedziak, G.L. Brett, D.R. Jones, X. Liu, J.K. Edwards, D.J. Morgan, D.K. Knight, G.J. Hutchings, Pd-Ru/TiO_2 catalyst-an active and selective catalyst for furfural hydrogenation, Catal. Sci. Technol. 6 (2016) 234–242.
[24] W. Yu, K. Xiong, N. Ji, M.D. Porosoff, J.G. Chen, Theoretical and experimental studies of the adsorption geometry and reaction pathways of furfural over FeNi bimetallic model surfaces and supported catalysts, J. Catal. 317 (2014) 253–262.
[25] N. Pino, S. Sitthisa, Q. Tan, T. Souza, D. López, D.E. Resasco, Structure, activity, and selectivity of bimetallic Pd-Fe/SiO_2 and Pd-Fe/γ-Al_2O_3 catalysts for the conversion of furfural, J. Catal. 350 (2017) 30–40.
[26] B. Seemala, C.M. Cai, C.E. Wyman, P. Christopher, Support induced control of surface composition in Cu-Ni/TiO_2 catalysts enables high yield co-conversion of HMF and furfural to methylated furans, ACS Catal. 7 (2017) 4070–4082.
[27] W. Liu, Y. Yang, L. Chen, E. Xu, J. Xu, S. Hong, X. Zhang, M. Wei, Atomically-ordered active sites in NiMo intermetallic compound toward low-pressure hydrodeoxygenation of furfural, Appl. Catal. B Environ. 282 (2021), 119569.
[28] J. Osswald, K. Kovnir, M. Armbruster, R. Giedigkeit, R. Jentoft, U. Wild, Y. Grin, R. Schlogl, Palladium–gallium intermetallic compounds for the selective hydrogenation of acetylenePart II: surface characterization and catalytic performance, J. Catal. 258 (2008) 219–227.
[29] J. Yu, Y. Yang, L. Chen, Z. Li, W. Liu, E. Xu, Y. Zhang, S. Hong, X. Zhang, M. Wei, NiBi intermetallic compounds catalyst toward selective hydrogenation of unsaturated aldehydes, Appl. Catal. B Environ. 277 (2020), 119273.
[30] H. Tian, X. Li, S. Chen, L. Zeng, J. Gong, Role of Sn in Ni-Sn/CeO_2 catalysts for ethanol steam reforming, Chin. J. Chem. 35 (2017) 651–658.
[31] J.W. Shabaker, G.W. Huber, J.A. Dumesic, Aqueous-phase reforming of oxygenated hydrocarbons over Sn-modified Ni catalysts, J. Catal. 222 (2004) 180–191.
[32] A. Onda, T. Komatsu, T. Yashima, Characterizations and catalytic properties of fine particles of Ni-Sn intermetallic compounds supported on SiO_2, J. Catal. 221 (2004) 378–385.
[33] L. Wang, E. Guan, J. Zhang, J. Yang, Y. Zhu, Y. Han, M. Yang, C. Cen, G. Fu, B. C. Gates, F.S. Xiao, Single-site catalyst promoters accelerate metal-catalyzed nitroarene hydrogenation, Nat. Commun. 9 (2018) 1362.
[34] G. Kresse, J. Furthmüller, Efficient iterative schemes for ab initio total-energy calculation using a plane-wave basis set, Phys. Rev. B 54 (1996) 11169–11186.
[35] G. Kresse, J. Furthmüller, Efficiency of ab-initio total energy calculations for metals and semiconductors using a plane-wave basis set, Comput. Mater. Sci. 6 (1996) 15–50.
[36] P.E. Blöchl, Projector augmented-wave method, Phys. Rev. B 50 (1994) 17953–17979.
[37] J.P. Perdew, K. Burke, M. Ernzerhof, Generalized gradient approximation made simple, Phys. Rev. Lett. 77 (1996) 3865–3868.
[38] D.M. Rao, T. Sun, Y.S. Yang, P. Yin, M. Pu, H. Yan, M. Wei, Theoretical study on the reaction mechanism and selectivity of acetylene semi-hydrogenation on Ni-Sn intermetallic catalysts, Phys. Chem. Chem. Phys. 21 (2019) 1384–1392.
[39] Y. Yang, L. Chen, Y. Chen, W. Liu, H. Feng, B. Wang, X. Zhang, M. Wei, The selective hydrogenation of furfural over intermetallic compounds with outstanding catalytic performance, Green Chem. 21 (2019) 5352–5362.
[40] H. He, S. Xia, D. Luo, Sn-assisted nickel synergistically catalyzes the direct cleavage of C_{Ar}-O bond in lignin-derived m-cresol: theoretical and experimental analysis, J. Catal. 410 (2022) 180–193.
[41] T. Stroud, T.J. Smith, E. Le Saché, J.L. Santos, M.A. Centeno, H. Arellano-Garcia, J. A. Odriozola, T.R. Reina, Chemical CO_2 recycling via dry and bi reforming of methane using Ni-Sn/Al_2O_3 and Ni-Sn/CeO_2-Al_2O_3 catalysts, Appl. Catal. B Environ. 224 (2018) 125–135.
[42] F. Yang, D. Liu, H. Wang, X. Liu, J. Han, Q. Ge, X. Zhu, Geometric and electronic effects of bimetallic Ni-Re catalysts for selective deoxygenation of m-cresol to toluene, J. Catal. 349 (2017) 84–97.
[43] F. Yang, M.R. Komarneni, N.J. Libretto, L. Li, W. Zhou, J.T. Miller, Q. Ge, X. Zhu, D. E. Resasco, Elucidating the structure of bimetallic NiW/SiO_2 catalysts and its consequences on selective deoxygenation of m-cresol to toluene, ACS Catal. 11 (2021) 2935–2948.
[44] U. Guharoy, E. Le Saché, Q. Cai, T.R. Reina, S. Gu, Understanding the role of Ni-Sn interaction to design highly effective CO_2 conversion catalysts for dry reforming of methane, J. CO_2 Util. 27 (2018) 1–10.
[45] X. Zhu, Y. Zhang, C. Liu, CO adsorbed infrared spectroscopy study of Ni/Al_2O_3 catalyst for CO_2 reforming of methane, Catal. Lett. 118 (2007) 306–312.
[46] D.G. Blackmond, E.I. Ko, Structural sensitivity of CO adsorption and H_2 CO coadsorption on Ni/SiO_2 catalysts, J. Catal. 96 (1985) 210–221.
[47] Y. Yao, D.W. Goodman, In situ IR spectroscopic studies of Ni surface segregation induced by CO adsorption on Cu-Ni/SiO_2 bimetallic catalysts, Phys. Chem. Chem. Phys. 16 (2014) 3823–3829.
[48] M. Primet, Electronic transfer and ligand effects in the infrared spectra of adsorbed carbon monoxide, J. Catal. 88 (1984) 273–282.
[49] F.J.C.M. Toolenaar, F. Stoop, V. Ponec, On electronic and geometric effects of alloying-an infrared spectroscopic investigation of the adsorption of carbon monoxide on Platinum-Copper alloys, J. Catal. 82 (1983) 1–12.
[50] J. Shabaker, D. Simonetti, R. Cortright, J. Dumesic, Sn-modified Ni catalysts for aqueous-phase reforming: characterization and deactivation studies, J. Catal. 231 (2005) 67–76.
[51] G. Aguilar-Rios, M. Valenzuela, P. Salas, H. Armendariz, P. Bosch, G.D. Toro, R. Silva, V. Bertin, S. Castillo, A. Ramirez-Solis, I. Schifter, Hydrogen interactions and catalytic properties of Pt-Sn supported on zinc aluminate, Appl. Catal. A Gen. 127 (1995) 65–75.
[52] X. Zhu, L.L. Lobban, R.G. Mallinson, D.E. Resasco, Bifunctional transalkylation and hydrodeoxygenation of anisole over a Pt/HBeta catalyst, J. Catal. 281 (2011) 21–29.
[53] C.P. Jimenez-Gomez, J.A. Cecilia, R. Moreno-Tost, P. Maireles-Torres, Nickel phosphide/silica catalysts for the gas-phase hydrogenation of furfural to high-added-value chemicals, ChemCatChem 9 (2017) 2881–2889.
[54] E. Nikolla, A. Holewinski, J. Schwank, S. Linic, Controlling carbon surface chemistry by alloying: carbon tolerant reforming catalyst, J. Am. Chem. Soc. 128 (2006) 11354–11355.
[55] F. Yang, N.J. Libretto, M.R. Komarneni, W. Zhou, J.T. Miller, X. Zhu, D.E. Resasco, Enhancement of m-cresol hydrodeoxygenation selectivity on Ni catalysts by surface decoration of MoO_x species, ACS Catal. (2019) 7791–7800.
[56] C.A. Teles, P.M. de Souza, A.H. Braga, R.C. Rabelo-Neto, A. Teran, G. Jacobs, D. E. Resasco, F.B. Noronha, The role of defect sites and oxophilicity of the support on the phenol hydrodeoxygenation reaction, Appl. Catal. B Environ. 249 (2019) 292–305.